

## 2 In-situ calibration of the single-photoelectron charge 3 response of the IceCube photomultiplier tubes

---



4 ICECUBE

### 5 IceCube collaboration

6 M. G. Aartsen,<sup>p</sup> M. Ackermann,<sup>bc</sup> J. Adams,<sup>p</sup> J. A. Aguilar,<sup>l</sup> M. Ahlers,<sup>t</sup> M. Ahrens,<sup>at</sup>  
7 C. Alispach,<sup>z</sup> K. Andeen,<sup>ak</sup> T. Anderson,<sup>az</sup> I. Ansseau,<sup>l</sup> G. Anton,<sup>x</sup> C. Argüelles,<sup>n</sup>  
8 J. Auffenberg,<sup>a</sup> S. Axani,<sup>n</sup> P. Backes,<sup>a</sup> H. Bagherpour,<sup>p</sup> X. Bai,<sup>aq</sup> A. Balagopal V.,<sup>ac</sup>  
9 A. Barbano,<sup>z</sup> S. W. Barwick,<sup>ab</sup> B. Bastian,<sup>bc</sup> V. Baum,<sup>aj</sup> S. Baur,<sup>l</sup> R. Bay,<sup>h</sup> J. J. Beatty,<sup>r,s</sup>  
10 K.-H. Becker,<sup>bb</sup> J. Becker Tjus,<sup>k</sup> S. BenZvi,<sup>as</sup> D. Berley,<sup>q</sup> E. Bernardini,<sup>bc,bd</sup>  
11 D. Z. Besson,<sup>ad,be</sup> G. Binder,<sup>h,i</sup> D. Bindig,<sup>bb</sup> E. Blaufuss,<sup>q</sup> S. Blot,<sup>bc</sup> C. Boehm,<sup>at</sup> M. Börner,<sup>u</sup>  
12 S. Böser,<sup>aj</sup> O. Botner,<sup>ba</sup> J. Böttcher,<sup>a</sup> E. Bourbeau,<sup>t</sup> J. Bourbeau,<sup>ai</sup> F. Bradascio,<sup>bc</sup>  
13 J. Braun,<sup>ai</sup> S. Bron,<sup>z</sup> J. Brostean-Kaiser,<sup>bc</sup> A. Burgman,<sup>ba</sup> J. Buscher,<sup>a</sup> R. S. Busse,<sup>al</sup>  
14 T. Carver,<sup>z</sup> C. Chen,<sup>f</sup> E. Cheung,<sup>q</sup> D. Chirkin,<sup>ai</sup> S. Choi,<sup>av</sup> K. Clark,<sup>ae</sup> L. Classen,<sup>al</sup>  
15 A. Coleman,<sup>am</sup> G. H. Collin,<sup>n</sup> J. M. Conrad,<sup>n</sup> P. Coppin,<sup>m</sup> P. Correa,<sup>m</sup> D. F. Cowen,<sup>ay,az</sup>  
16 R. Cross,<sup>as</sup> P. Dave,<sup>f</sup> C. De Clercq,<sup>m</sup> J. J. DeLaunay,<sup>az</sup> H. Dembinski,<sup>am</sup> K. Deoskar,<sup>at</sup>  
17 S. De Ridder,<sup>aa</sup> P. Desiati,<sup>ai</sup> K. D. de Vries,<sup>m</sup> G. de Wasseige,<sup>m</sup> M. de With,<sup>j</sup> T. DeYoung,<sup>v</sup>  
18 A. Diaz,<sup>n</sup> J. C. Díaz-Vélez,<sup>ai</sup> H. Dujmovic,<sup>av</sup> M. Dunkman,<sup>az</sup> E. Dvorak,<sup>aq</sup> B. Eberhardt,<sup>ai</sup>  
19 T. Ehrhardt,<sup>aj</sup> P. Eller,<sup>az</sup> R. Engel,<sup>ac</sup> P. A. Evenson,<sup>am</sup> S. Fahey,<sup>ai</sup> A. R. Fazely,<sup>g</sup> J. Felde,<sup>q</sup>  
20 K. Filimonov,<sup>h</sup> C. Finley,<sup>at</sup> D. Fox,<sup>ay</sup> A. Franckowiak,<sup>bc</sup> E. Friedman,<sup>q</sup> A. Fritz,<sup>aj</sup>  
21 T. K. Gaisser,<sup>am</sup> J. Gallagher,<sup>ah</sup> E. Ganster,<sup>a</sup> S. Garrappa,<sup>bc</sup> L. Gerhardt,<sup>i</sup> K. Ghorbani,<sup>ai</sup>  
22 T. Glauch,<sup>y</sup> T. Glüsenkamp,<sup>x</sup> A. Goldschmidt,<sup>i</sup> J. G. Gonzalez,<sup>am</sup> D. Grant,<sup>v</sup> Z. Griffith,<sup>ai</sup>  
23 S. Griswold,<sup>as</sup> M. Günder,<sup>a</sup> M. Gündüz,<sup>k</sup> C. Haack,<sup>a</sup> A. Hallgren,<sup>ba</sup> L. Halve,<sup>a</sup> F. Halzen,<sup>ai</sup>  
24 K. Hanson,<sup>ai</sup> A. Haungs,<sup>ac</sup> D. Hebecker,<sup>j</sup> D. Heereman,<sup>l</sup> P. Heix,<sup>a</sup> K. Helbing,<sup>bb</sup> R. Hellauer,<sup>q</sup>  
25 F. Henningsen,<sup>y</sup> S. Hickford,<sup>bb</sup> J. Hignight,<sup>w</sup> G. C. Hill,<sup>b</sup> K. D. Hoffman,<sup>q</sup> R. Hoffmann,<sup>bb</sup>  
26 T. Hoinka,<sup>u</sup> B. Hokanson-Fasig,<sup>ai</sup> K. Hoshina,<sup>ai,be</sup> F. Huang,<sup>az</sup> M. Huber,<sup>y</sup> T. Huber,<sup>ac,bc</sup>  
27 K. Hultqvist,<sup>at</sup> M. Hünnefeld,<sup>u</sup> R. Hussain,<sup>ai</sup> S. In,<sup>av</sup> N. Iovine,<sup>l</sup> A. Ishihara,<sup>o</sup> G. S. Japaridze,<sup>e</sup>  
28 M. Jeong,<sup>av</sup> K. Jero,<sup>ai</sup> B. J. P. Jones,<sup>d</sup> F. Jonske,<sup>a</sup> R. Joppe,<sup>a</sup> D. Kang,<sup>ac</sup> W. Kang,<sup>av</sup>  
29 A. Kappes,<sup>al</sup> D. Kappesser,<sup>aj</sup> T. Karg,<sup>bc</sup> M. Karl,<sup>y</sup> A. Karle,<sup>ai</sup> U. Katz,<sup>x</sup> M. Kauer,<sup>ai</sup>  
30 J. L. Kelley,<sup>ai</sup> A. Kheirandish,<sup>ai</sup> J. Kim,<sup>av</sup> T. Kintscher,<sup>bc</sup> J. Kiryluk,<sup>au</sup> T. Kittler,<sup>x</sup>  
31 S. R. Klein,<sup>h,i</sup> R. Koirala,<sup>am</sup> H. Kolanoski,<sup>j</sup> L. Köpke,<sup>aj</sup> C. Kopper,<sup>v</sup> S. Kopper,<sup>ax</sup>  
32 D. J. Koskinen,<sup>t</sup> M. Kowalski,<sup>j,bc</sup> K. Krings,<sup>y</sup> G. Krückl,<sup>aj</sup> N. Kulacz,<sup>w</sup> N. Kurahashi,<sup>ap</sup>  
33 A. Kyriacou,<sup>b</sup> M. Labare,<sup>aa</sup> J. L. Lanfranchi,<sup>az</sup> M. J. Larson,<sup>q</sup> F. Lauber,<sup>bb</sup> J. P. Lazar,<sup>ai</sup>  
34 K. Leonard,<sup>ai</sup> A. Leszczyńska,<sup>ac</sup> M. Leuermann,<sup>a</sup> Q. R. Liu,<sup>ai</sup> E. Lohfink,<sup>aj</sup>

35 C. J. Lozano Mariscal,<sup>al</sup> L. Lu,<sup>o</sup> F. Lucarelli,<sup>z</sup> J. Lünemann,<sup>m</sup> W. Luszczak,<sup>ai</sup> Y. Lyu,<sup>h,i</sup>  
 36 W. Y. Ma,<sup>bc</sup> J. Madsen,<sup>ar</sup> G. Maggi,<sup>m</sup> K. B. M. Mahn,<sup>v</sup> Y. Makino,<sup>o</sup> P. Mallik,<sup>a</sup> K. Mallot,<sup>ai</sup>  
 37 S. Mancina,<sup>ai</sup> I. C. Mariş,<sup>l</sup> R. Maruyama,<sup>an</sup> K. Mase,<sup>o</sup> R. Maunu,<sup>q</sup> F. McNally,<sup>ag</sup> K. Meagher,<sup>ai</sup>  
 38 M. Medici,<sup>t</sup> A. Medina,<sup>s</sup> M. Meier,<sup>u</sup> S. Meighen-Berger,<sup>y</sup> T. Menne,<sup>u</sup> G. Merino,<sup>ai</sup> T. Meures,<sup>l</sup>  
 39 J. Micallef,<sup>v</sup> D. Mockler,<sup>l</sup> G. Momenté,<sup>aj</sup> T. Montaruli,<sup>z</sup> R. W. Moore,<sup>w</sup> R. Morse,<sup>ai</sup> M. Moulai,<sup>n</sup>  
 40 P. Muth,<sup>a</sup> R. Nagai,<sup>o</sup> U. Naumann,<sup>bb</sup> G. Neer,<sup>v</sup> H. Niederhausen,<sup>y</sup> M. U. Nisa,<sup>v</sup> S. C. Nowicki,<sup>v</sup>  
 41 D. R. Nygren,<sup>i</sup> A. Obertacke Pollmann,<sup>bb</sup> M. Oehler,<sup>ac</sup> A. Olivas,<sup>q</sup> A. O’Murchadha,<sup>l</sup>  
 42 E. O’Sullivan,<sup>at</sup> T. Palczewski,<sup>h,i</sup> H. Pandya,<sup>am</sup> D. V. Pankova,<sup>az</sup> N. Park,<sup>ai</sup> P. Peiffer,<sup>aj</sup>  
 43 C. Pérez de los Heros,<sup>ba</sup> S. Philippen,<sup>a</sup> D. Pieloth,<sup>u</sup> E. Pinat,<sup>l</sup> A. Pizzuto,<sup>ai</sup> M. Plum,<sup>ak</sup>  
 44 A. Porcelli,<sup>aa</sup> P. B. Price,<sup>h</sup> G. T. Przybylski,<sup>i</sup> C. Raab,<sup>l</sup> A. Raissi,<sup>p</sup> M. Rameez,<sup>t</sup> L. Rauch,<sup>bc</sup>  
 45 K. Rawlins,<sup>c</sup> I. C. Rea,<sup>y</sup> R. Reimann,<sup>a</sup> B. Relethford,<sup>ap</sup> M. Renschler,<sup>ac</sup> G. Renzi,<sup>l</sup>  
 46 E. Resconi,<sup>y</sup> W. Rhode,<sup>u</sup> M. Richman,<sup>ap</sup> S. Robertson,<sup>i</sup> M. Rongen,<sup>a</sup> C. Rott,<sup>av</sup> T. Ruhe,<sup>u</sup>  
 47 D. Ryckbosch,<sup>aa</sup> D. Rysewyk,<sup>v</sup> I. Safa,<sup>ai</sup> S. E. Sanchez Herrera,<sup>v</sup> A. Sandrock,<sup>u</sup>  
 48 J. Sandros,<sup>aj</sup> M. Santander,<sup>ax</sup> S. Sarkar,<sup>ao</sup> S. Sarkar,<sup>w</sup> K. Satalecka,<sup>bc</sup> M. Schaufel,<sup>a</sup>  
 49 H. Schieler,<sup>ac</sup> P. Schlunder,<sup>u</sup> T. Schmidt,<sup>q</sup> A. Schneider,<sup>ai</sup> J. Schneider,<sup>x</sup>  
 50 F. G. Schröder,<sup>ac,am</sup> L. Schumacher,<sup>a</sup> S. Sclafani,<sup>ap</sup> D. Seckel,<sup>am</sup> S. Seunarine,<sup>ar</sup>  
 51 S. Shefali,<sup>a</sup> M. Silva,<sup>ai</sup> R. Snihur,<sup>ai</sup> J. Soedingrekso,<sup>u</sup> D. Soldin,<sup>am</sup> M. Song,<sup>q</sup>  
 52 G. M. Spiczak,<sup>ar</sup> C. Spiering,<sup>bc</sup> J. Stachurska,<sup>bc</sup> M. Stamatikos,<sup>s</sup> T. Stanev,<sup>am</sup> R. Stein,<sup>bc</sup>  
 53 P. Steinmüller,<sup>ac</sup> J. Stettner,<sup>a</sup> A. Steuer,<sup>aj</sup> T. Stezelberger,<sup>i</sup> R. G. Stokstad,<sup>i</sup> A. Stöbl,<sup>o</sup>  
 54 N. L. Strotjohann,<sup>bc</sup> T. Stürwald,<sup>a</sup> T. Stuttard,<sup>t</sup> G. W. Sullivan,<sup>q</sup> I. Taboada,<sup>f</sup> F. Tenholt,<sup>k</sup>  
 55 S. Ter-Antonyan,<sup>g</sup> A. Terliuk,<sup>bc</sup> S. Tilav,<sup>am</sup> K. Tollefson,<sup>v</sup> L. Tomankova,<sup>k</sup> C. Tönnis,<sup>aw</sup>  
 56 S. Toscano,<sup>l</sup> D. Tosi,<sup>ai</sup> A. Trettin,<sup>bc</sup> M. Tselengidou,<sup>x</sup> C. F. Tung,<sup>f</sup> A. Turcati,<sup>y</sup> R. Turcotte,<sup>ac</sup>  
 57 C. F. Turley,<sup>az</sup> B. Ty,<sup>ai</sup> E. Unger,<sup>ba</sup> M. A. Unland Elorrieta,<sup>al</sup> M. Usner,<sup>bc</sup> J. Vandenbroucke,<sup>ai</sup>  
 58 W. Van Driessche,<sup>aa</sup> D. van Eijk,<sup>ai</sup> N. van Eijndhoven,<sup>m</sup> S. Vanheule,<sup>aa</sup> J. van Santen,<sup>bc</sup>  
 59 M. Vraeghe,<sup>aa</sup> C. Walck,<sup>at</sup> A. Wallace,<sup>b</sup> M. Wallraff,<sup>a</sup> N. Wandkowsky,<sup>ai</sup> T. B. Watson,<sup>d</sup>  
 60 C. Weaver,<sup>w</sup> A. Weindl,<sup>ac</sup> M. J. Weiss,<sup>az</sup> J. Weldert,<sup>aj</sup> C. Wendt,<sup>ai</sup> J. Werthebach,<sup>ai</sup>  
 61 B. J. Whelan,<sup>b</sup> N. Whitehorn,<sup>af</sup> K. Wiebe,<sup>aj</sup> C. H. Wiebusch,<sup>a</sup> L. Wille,<sup>ai</sup> D. R. Williams,<sup>ax</sup>  
 62 L. Wills,<sup>ap</sup> M. Wolf,<sup>y</sup> J. Wood,<sup>ai</sup> T. R. Wood,<sup>w</sup> K. Woschnagg,<sup>h</sup> G. Wrede,<sup>x</sup> D. L. Xu,<sup>ai</sup>  
 63 X. W. Xu,<sup>g</sup> Y. Xu,<sup>au</sup> J. P. Yanez,<sup>w</sup> G. Yodh,<sup>ab</sup> S. Yoshida,<sup>o</sup> T. Yuan<sup>ai</sup> and M. Zöcklein<sup>a</sup>

64 <sup>a</sup>*III. Physikalisches Institut, RWTH Aachen University, D-52056 Aachen, Germany*

65 <sup>b</sup>*Department of Physics, University of Adelaide, Adelaide, 5005, Australia*

66 <sup>c</sup>*Dept. of Physics and Astronomy, University of Alaska Anchorage, 3211 Providence Dr., Anchorage, AK*  
 67 *99508, USA*

68 <sup>d</sup>*Dept. of Physics, University of Texas at Arlington, 502 Yates St., Science Hall Rm 108, Box 19059,*  
 69 *Arlington, TX 76019, USA*

70 <sup>e</sup>*CTSPS, Clark-Atlanta University, Atlanta, GA 30314, USA*

71 <sup>f</sup>*School of Physics and Center for Relativistic Astrophysics, Georgia Institute of Technology, Atlanta, GA*  
 72 *30332, USA*

73 <sup>g</sup>*Dept. of Physics, Southern University, Baton Rouge, LA 70813, USA*

74 <sup>h</sup>*Dept. of Physics, University of California, Berkeley, CA 94720, USA*

75 <sup>i</sup>*Lawrence Berkeley National Laboratory, Berkeley, CA 94720, USA*

76 <sup>j</sup>*Institut für Physik, Humboldt-Universität zu Berlin, D-12489 Berlin, Germany*

77 <sup>k</sup>*Fakultät für Physik & Astronomie, Ruhr-Universität Bochum, D-44780 Bochum, Germany*

78 <sup>l</sup> *Université Libre de Bruxelles, Science Faculty CP230, B-1050 Brussels, Belgium*  
79 <sup>m</sup> *Vrije Universiteit Brussel (VUB), Dienst ELEM, B-1050 Brussels, Belgium*  
80 <sup>n</sup> *Dept. of Physics, Massachusetts Institute of Technology, Cambridge, MA 02139, USA*  
81 <sup>o</sup> *Dept. of Physics and Institute for Global Prominent Research, Chiba University, Chiba 263-8522, Japan*  
82 <sup>p</sup> *Dept. of Physics and Astronomy, University of Canterbury, Private Bag 4800, Christchurch, New Zealand*  
83 <sup>q</sup> *Dept. of Physics, University of Maryland, College Park, MD 20742, USA*  
84 <sup>r</sup> *Dept. of Astronomy, Ohio State University, Columbus, OH 43210, USA*  
85 <sup>s</sup> *Dept. of Physics and Center for Cosmology and Astro-Particle Physics, Ohio State University, Columbus,*  
86 *OH 43210, USA*  
87 <sup>t</sup> *Niels Bohr Institute, University of Copenhagen, DK-2100 Copenhagen, Denmark*  
88 <sup>u</sup> *Dept. of Physics, TU Dortmund University, D-44221 Dortmund, Germany*  
89 <sup>v</sup> *Dept. of Physics and Astronomy, Michigan State University, East Lansing, MI 48824, USA*  
90 <sup>w</sup> *Dept. of Physics, University of Alberta, Edmonton, Alberta, Canada T6G 2E1*  
91 <sup>x</sup> *Erlangen Centre for Astroparticle Physics, Friedrich-Alexander-Universität Erlangen-Nürnberg, D-91058*  
92 *Erlangen, Germany*  
93 <sup>y</sup> *Physik-department, Technische Universität München, D-85748 Garching, Germany*  
94 <sup>z</sup> *Département de physique nucléaire et corpusculaire, Université de Genève, CH-1211 Genève, Switzerland*  
95 <sup>aa</sup> *Dept. of Physics and Astronomy, University of Gent, B-9000 Gent, Belgium*  
96 <sup>ab</sup> *Dept. of Physics and Astronomy, University of California, Irvine, CA 92697, USA*  
97 <sup>ac</sup> *Karlsruhe Institute of Technology, Institut für Kernphysik, D-76021 Karlsruhe, Germany*  
98 <sup>ad</sup> *Dept. of Physics and Astronomy, University of Kansas, Lawrence, KS 66045, USA*  
99 <sup>ae</sup> *SNOLAB, 1039 Regional Road 24, Creighton Mine 9, Lively, ON, Canada P3Y 1N2*  
100 <sup>af</sup> *Department of Physics and Astronomy, UCLA, Los Angeles, CA 90095, USA*  
101 <sup>ag</sup> *Department of Physics, Mercer University, Macon, GA 31207-0001, USA*  
102 <sup>ah</sup> *Dept. of Astronomy, University of Wisconsin, Madison, WI 53706, USA*  
103 <sup>ai</sup> *Dept. of Physics and Wisconsin IceCube Particle Astrophysics Center, University of Wisconsin, Madison,*  
104 *WI 53706, USA*  
105 <sup>aj</sup> *Institute of Physics, University of Mainz, Staudinger Weg 7, D-55099 Mainz, Germany*  
106 <sup>ak</sup> *Department of Physics, Marquette University, Milwaukee, WI, 53201, USA*  
107 <sup>al</sup> *Institut für Kernphysik, Westfälische Wilhelms-Universität Münster, D-48149 Münster, Germany*  
108 <sup>am</sup> *Bartol Research Institute and Dept. of Physics and Astronomy, University of Delaware, Newark, DE 19716,*  
109 *USA*  
110 <sup>an</sup> *Dept. of Physics, Yale University, New Haven, CT 06520, USA*  
111 <sup>ao</sup> *Dept. of Physics, University of Oxford, Parks Road, Oxford OX1 3PU, UK*  
112 <sup>ap</sup> *Dept. of Physics, Drexel University, 3141 Chestnut Street, Philadelphia, PA 19104, USA*  
113 <sup>aq</sup> *Physics Department, South Dakota School of Mines and Technology, Rapid City, SD 57701, USA*  
114 <sup>ar</sup> *Dept. of Physics, University of Wisconsin, River Falls, WI 54022, USA*  
115 <sup>as</sup> *Dept. of Physics and Astronomy, University of Rochester, Rochester, NY 14627, USA*  
116 <sup>at</sup> *Oskar Klein Centre and Dept. of Physics, Stockholm University, SE-10691 Stockholm, Sweden*  
117 <sup>au</sup> *Dept. of Physics and Astronomy, Stony Brook University, Stony Brook, NY 11794-3800, USA*  
118 <sup>av</sup> *Dept. of Physics, Sungkyunkwan University, Suwon 16419, Korea*  
119 <sup>aw</sup> *Institute of Basic Science, Sungkyunkwan University, Suwon 16419, Korea*  
120 <sup>ax</sup> *Dept. of Physics and Astronomy, University of Alabama, Tuscaloosa, AL 35487, USA*  
121 <sup>ay</sup> *Dept. of Astronomy and Astrophysics, Pennsylvania State University, University Park, PA 16802, USA*

122 <sup>az</sup>*Dept. of Physics, Pennsylvania State University, University Park, PA 16802, USA*

123 <sup>ba</sup>*Dept. of Physics and Astronomy, Uppsala University, Box 516, S-75120 Uppsala, Sweden*

124 <sup>bb</sup>*Dept. of Physics, University of Wuppertal, D-42119 Wuppertal, Germany*

125 <sup>bc</sup>*DESY, D-15738 Zeuthen, Germany*

126 <sup>bd</sup>*also at Università di Padova, I-35131 Padova, Italy*

127 <sup>be</sup>*also at National Research Nuclear University, Moscow Engineering Physics Institute (MEPhI), Moscow*  
128 *115409, Russia*

129 <sup>bf</sup>*Earthquake Research Institute, University of Tokyo, Bunkyo, Tokyo 113-0032, Japan*

130 *E-mail: [analysis@icecube.wisc.edu](mailto:analysis@icecube.wisc.edu)*

131 **ABSTRACT:** We describe an improved in-situ calibration of the single-photoelectron charge distri-  
132 **butions** for each of the in-ice Hamamatsu Photonics R7081-02[MOD] photomultiplier tubes in the  
133 **IceCube Neutrino Observatory.** The characterization of the individual PMT charge distributions is  
134 **important** for PMT calibration, data and Monte Carlo simulation agreement, and understanding the  
135 **effect** of hardware differences within the detector. We discuss the single photoelectron identification  
136 **procedure** and how we extract the single-photoelectron charge distribution using a deconvolution  
137 **of the multiple-photoelectron charge distribution.**

138 **KEYWORDS:** IceCube, single-photoelectron charge distribution, photomultiplier tubes, calibration

139 **ARXIV EPRINT:** [tbd](#)

---

## 140 Contents

141	<b>1 Introduction</b>	<b>1</b>
142	1.1 Single-photoelectron charge distributions	4
143	1.2 IceCube datasets and software definitions	6
144	<b>2 Extracting the SPE charge templates</b>	<b>7</b>
145	2.1 Single photoelectron pulse selection	7
146	2.2 Characterizing the low-charge region	8
147	2.3 Fitting procedure	10
148	2.4 SPE charge template fit results	10
149	<b>3 Discussion</b>	<b>12</b>
150	3.1 Correlations between fit parameters and DOM hardware differences	12
151	3.2 Fitting parameters variation over time	14
152	3.3 Quantifying observable changes when modifying the PMT charge distributions	15
153	3.3.1 Model comparison	16
154	3.4 SPE charge templates for calibration	17
155	3.5 SPE charge templates in simulation	17
156	<b>4 Conclusion</b>	<b>17</b>

---

## 157 1 Introduction

158 The IceCube Neutrino Observatory [1, 2] is a cubic-kilometer-sized array of 5,160 photomultiplier  
159 tubes (PMTs) buried in the Antarctic ice sheet, designed to observe high-energy neutrinos interacting  
160 with the ice [3]. In 2011, the IceCube Collaboration completed the installation of 86 vertical *strings*  
161 of PMT modules, eight of which were arranged in a denser configuration known as the DeepCore  
162 sub-array [4]. Each string in IceCube contains 60 digital optical modules (DOMs), which contain  
163 a single PMT each, as well as all required electronics [5]. The primary 78 strings (excluding  
164 DeepCore) are spaced 125 m apart in a hexagonal grid, with the DOMs extending from 1450 m to  
165 2450 m below the surface of the ice sheet. The additional DeepCore strings (79-86) are positioned  
166 between the centermost strings in the detector, reducing the horizontal DOM-to-DOM distance  
167 in this region to between 42 m and 72 m. The lower 50 DOMs on these strings are located in  
168 the deepest 350 m of the detector surrounded by the cleanest ice [6], while the upper ten provide  
169 a cosmic ray veto extending down from 1900 m to 2000 m below the surface. Above the in-ice  
170 detectors, there exists a surface array, IceTop [7], consisting of 81 stations located just above the  
171 in-ice IceCube strings. The PMTs located in IceTop DOMs operate at a lower gain and the data  
172 from these PMTs was not included in the current analysis; however, the IceTop PMTs are calibrated

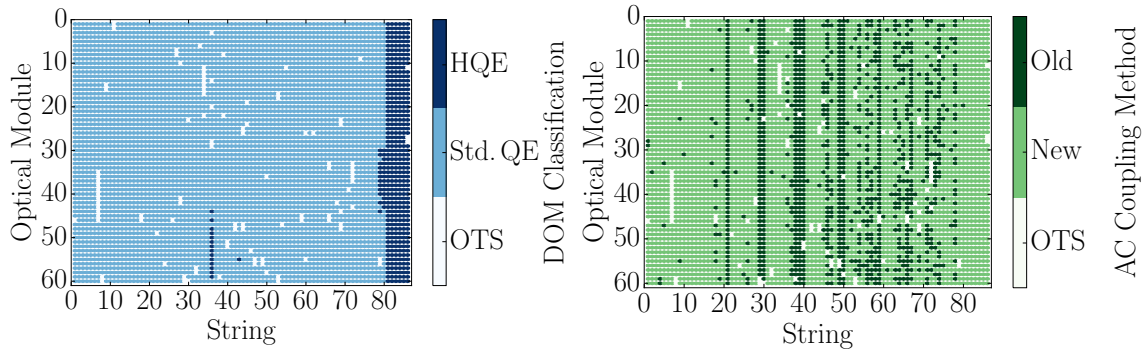


**Figure 1.** Left: A mapping of the HQE (dark blue) and Standard QE DOMs (light blue). Right: The version of AC coupling, old toroids (dark green) and new toroids (light green). DOMs that have been removed from service (OTS) are shown in white. These are primarily DOMs that resulted in failures during deployment and freeze-in, and failures during subsequent operation, as described in Ref. [9].

173 to single photoelectron charge distribution in a similar way as the in-ice PMTs (see Sec. 5.1 in  
174 Ref. [7]).

175 Each DOM consists of a 0.5"-thick spherical glass pressure vessel that houses a single down-  
176 facing 10" PMT from Hamamatsu Photonics. The PMT is coupled to the glass housing with optical  
177 gel and is surrounded by a wire mesh to reduce the effect of the Earth's ambient magnetic field.  
178 The glass housing is transparent to wavelengths of 350 nm and above [8].

179 Of the 5,160 DOMs, 4,762 house a R7081-02 Hamamatsu Photonics PMT, sensitive to wave-  
180 lengths ranging from 300 nm to 650 nm, with a peak quantum efficiency of 25% near 390 nm. These  
181 are classified as Standard Quantum Efficiency (Standard QE) DOMs. The remaining 398 DOMs  
182 are equipped with the Hamamatsu R7081-02MOD PMTs, which, having a peak quantum efficiency  
183 of 34% near 390 nm (36% higher efficiency than the Standard QE DOMs), are classified as High  
184 Quantum Efficiency (HQE) DOMs [4]. These DOMs are primarily located in DeepCore and on  
185 strings 36 and 43, as shown in the left side of Fig. 1.

186 The R7081-02 and R7081-02MOD PMTs have 10 dynode stages and are operated with a  
187 nominal gain of  $10^7$  and achieved with high voltages ranging from approximately  $1215 \pm 83$  V and  
188  $1309 \pm 72$  V, respectively. A typical amplified single photoelectron generates a  $5.2 \pm 0.3$  mV peak  
189 voltage after digitization with a full width at half maximum of  $13 \pm 1$  ns. The PMTs are operated  
190 with the anodes at high voltage, so the signal is AC coupled to the amplifiers (front-end amplifiers).  
191 There are two versions of AC coupling in the detectors, referred to as the *new* and *old toroids*, both  
192 of which use custom-designed wideband bifilar wound 1:1 toroidal transformers<sup>1</sup>. The locations of  
193 DOMs with the different versions of AC-coupling are shown on the right side of Fig. 1. The DOMs  
194 with the old toroids were designed with an impedance of  $43 \Omega$ , while the new toroids are  $50 \Omega$  [9].  
195 All HQE DOMs are instrumented with the new toroids.

196 IceCube relies on two observables per DOM to reconstruct events: the total number of detected

<sup>1</sup>The toroidal transformer effectively acts as a high-pass filter with good signal fidelity at high frequencies and offers a higher level of reliability than capacitive coupling. Conventional AC-coupling high-voltage ceramic capacitors can also produce undesirable noise from leakage currents and are impractical given the signal droop and undershoot requirements [8].

197 photons and their timing distribution. Both the timing and the number of photons are extracted  
198 from the digitized waveforms. This is accomplished by deconvolving the digitized waveforms [10]  
199 into a series of scaled single photoelectron pulses (so-called pulse series), and the integral of  
200 the individual pulses divided by the load resistance defines the observed charge. It will often be  
201 expressed in units of PE, or photoelectrons, which further divides the measured charge by the charge  
202 of a single electron times the nominal gain.

203 When one or more photoelectrons produce a voltage at the anode sufficient to trigger the  
204 onboard discriminator, the signal acquisition process is triggered. The discriminator threshold is  
205 set to approximately 1.2 mV, or equivalently to  $\sim 0.23$  PE, via a digital-to-analog converter (DAC).  
206 The signal is presented to four parallel channels for digitization. Three channels pass through a 75 ns  
207 delay loop in order to capture the waveform leading up to the rising edge of the triggering pulse, and  
208 are then subject to different levels of amplification prior to being digitized at 300 million samples  
209 per second (MSPS) for 128 samples using a 10-bit Analog Transient Waveform Digitizer (ATWD).  
210 The high-gain channel has a nominal amplification of 16 and is most suitable for single photon  
211 detection. Two ATWD chips are present on the DOM Mainboard (MB) and alternate digitization  
212 between waveforms to remove dead time associated with the readout. The signal to the fourth  
213 parallel channel is first shaped and amplified, then fed into a 10-bit fast analog-to-digital converter  
214 (fADC) operating at a sampling rate of 40 MSPS. Further detail regarding the description of the  
215 DOM electronics can be found in Refs. [5, 11].

216 This article discusses a method for determining the in-situ single-photoelectron charge dis-  
217 tributions of individual PMTs, which can be used to improve calibration and the overall detector  
218 description in Monte Carlo (MC) simulation. The SPE charge distribution refers to the charge  
219 probability density function of an individual PMT generated by the amplification of a pure sample  
220 of single photoelectrons. The measured shape of the SPE charge distributions is shown to be useful  
221 for examining hardware differences and assessing long term stability of the detector. This was made  
222 possible with the development of two pieces of software:

- 223 1. A specially-designed unbiased pulse selection developed to reduce the multiple photoelec-  
224 tron (MPE) contamination while accounting for other physical phenomena (e.g. late pulses,  
225 afterpulses, pre-pulses, and baseline shifts) and software-related effects (e.g. pulse splitting).  
226 This is further described in Sec. 2.1.
- 227 2. A fitting procedure developed to separate the remaining MPE contamination from the SPE  
228 charge distribution by deconvolving the measured charged distribution. This is further de-  
229 scribed in Sec. 2.3.

230 By using in-situ data to determine the SPE charge distributions, we accurately represent the  
231 individual PMT response as a function of time, environmental conditions, software version and  
232 hardware differences, and realistic photocathode illumination conditions. This is beneficial since  
233 it also allows us to inspect the stability and long-term behavior of the individual DOMs, verify  
234 previous calibration, and correlate features with specific DOM hardware.

## 235 1.1 Single-photoelectron charge distributions

236 Ideally, a single photon produces a single photoelectron, which is then amplified by a known  
237 amount, and the measured charge corresponds to 1 PE. However, there are many physical processes  
238 that create structure in the measured charge distributions. For example:

- 239 • **Statistical fluctuation due to cascade multiplication** [12]. At every stage of dynode  
240 amplification, the number of emitted electrons that make it to the next dynode is randomly  
241 distributed. This in turn causes a smearing in the measured charge after the gain stage of the  
242 PMT.
- 243 • **Photoelectron trajectory**. Some electrons may deviate from the favorable trajectory, re-  
244 ducing the number of secondaries produced at a dynode or the efficiency to collect them  
245 on the following dynode. This can occur at any stage, but it has the largest effect on the  
246 multiplication at the first dynode [13]. The trajectory of a photoelectron striking the first  
247 dynode will depend on many things, including where on the photocathode it was emitted,  
248 the uniformity of the electric field, the size and shape of the dynodes [12], and the ambient  
249 magnetic field [14, 15].
- 250 • **Late or delayed pulses**. A photoelectron can elastically or inelastically backscatter off the first  
251 dynode. The scattered electron can then be re-accelerated to the dynode, creating a second  
252 pulse. The difference in time between the initial pulse and the re-accelerated pulse in the  
253 R7081-02 PMT was previously measured to be up to 70 ns [8, 16]. Elastically backscattered  
254 photoelectrons will carry the full energy and are thus expected to produce similar charge to a  
255 non-backscattered photoelectron, albeit with a time offset. The mean measured charge of an  
256 inelastic backscattered photoelectron, by contrast, is expected to be smaller than a nominal  
257 photoelectron [17].
- 258 • **Afterpulses**. When photoelectrons or the secondary electrons produced during the electron  
259 cascade gain sufficient energy to ionize residual gas in the PMT, the resulting positively  
260 charged ionized gas will be accelerated in the electric field towards the photocathode. Upon  
261 impact with the photocathode, multiple electrons can be released from the photocathode,  
262 creating what is called an afterpulse. For the R7081-02 PMTs used in IceCube, the timescale  
263 for afterpulses was measured to occur from 0.3 to 11  $\mu$ s after the initial pulse, with the first  
264 prominent afterpulse peak occurring at approximately 600 ns [8]. The spread in the afterpulse  
265 time depends on the position of photocathode, the charge-to-mass ratio of the ion produced,  
266 and the electric potential distribution [18], whereas the size of the afterpulse is related to the  
267 momentum and species of the ionized gas and composition of the photocathode [19].
- 268 • **Pre-pulses**. If an incident photon passes through the photocathode without interaction and  
269 strikes the first dynode, it can eject an electron that is only amplified by the subsequent stages,  
270 resulting in a lower measured charge (lower by a factor of approximately 20). For the IceCube  
271 PMTs, the prepulses have been found to arrive approximately 30 ns before the signal from  
272 photoelectrons from the photocathode [8].

- 273 • **MPE contamination.** When multiple photoelectrons arrive at the first dynodes within few  
274 nanoseconds of each other, they can be reconstructed by the software as a single MPE pulse.
- 275 • **Dark noise.** Photoelectron emission, not initiated from an external event, can be attributed to  
276 thermionic emission from the low work function photocathode and the dynodes, Cherenkov  
277 radiations initiated from radioactive decay within the DOM, and field emission from the  
278 electrodes. Dark noise originating from thermionic emission from the dynodes is shown in  
279 Ref. [20] to populate the low-charge region.
- 280 • **Electronic noise.** This refers to the combined fluctuations caused by noise generated from the  
281 analog-frontend and the analog-to-digital converters (ATWDs and fADC). When integrated  
282 over a time window the resulting charge is generally small and centered around zero, thus  
283 only leading to a small broadening in the low charge region. The standard deviation of the  
284 electronic noise was found to be approximately  $\pm 0.11$  mV.

285 Beyond the physical phenomena above that modify the measured charge distribution, there is  
286 also a lower limit on the smallest charge that can be extracted. For IceCube, the discriminator only  
287 triggers for peak voltages above the threshold and subsequent pulses in the readout window are  
288 subject to a threshold defined in the software. This software threshold was set conservatively to  
289 avoid extracting pulses that originated from electronic noise. It can be modified to gain access to  
290 lower charge pulses and will be discussed in Sec. 2.2.

291 The standard SPE charge distribution used for all DOMs in IceCube, known as the TA0003  
292 distribution [8], models the above effects as the sum of an exponential plus a Gaussian. The  
293 TA0003 distribution is the average SPE charge distribution extracted from a lab measurement of  
294 118 Hamamatsu R7081-02 PMTs. The measurement was performed in a  $-32^\circ\text{C}$  freezer using a  
295 pulsed UV LED centered along the axis of the PMT, directly in front of the photocathode.

296 In 2013, IceCube has made several lab measurements of the SPE charge distribution of R7081-  
297 02 PMTs using single photons generated from synchronized short duration laser pulses. The  
298 coincident charge distribution generated by the laser pulses was found to include a steeply falling  
299 low-charge component in the region below the discriminator threshold. To account for this, a  
300 new functional form including a second exponential was introduced. This form of the normalized  
301 charge probability distribution  $f(q)_{\text{SPE}} = \text{Exp}_1 + \text{Exp}_2 + \text{Gaussian}$ , is referred to as the *SPE charge*  
302 *template* in this article. Explicitly, it is:

$$f(q)_{\text{SPE}} = \frac{P_{e1}}{w_1} \cdot e^{-q/w_1} + \frac{P_{e2}}{w_2} \cdot e^{-q/w_2} + \frac{1 - P_{e1} - P_{e2}}{\sigma \sqrt{\pi/2} \cdot \text{Erfc}[-\mu/(\sigma\sqrt{2})]} \cdot e^{-\frac{(q-\mu)^2}{2\sigma^2}}, \quad (1.1)$$

303 where  $q$  represents the measured charge;  $w_1$  and  $w_2$  are the exponential decay widths; and  $\mu$ ,  $\sigma$  are  
304 the Gaussian mean and width, respectively. The coefficients  $P_{e1}$ ,  $P_{e2}$ , and  $1 - P_{e1} - P_{e2}$  correspond  
305 to the probability of a photoelectron contributing to each component of the SPE template. The Erfc  
306 function used to normalize the Gaussian represents the complementary error function. Eq. 1.1 is  
307 the assumed functional shape of the SPE charge distributions, and the components of Eq. 1.1 are  
308 determined in this article for all in-ice DOMs. IceCube has chosen to define 1 PE as the location  
309 of the Gaussian mean ( $\mu$ ) and calibrates the gain of the individual PMTs prior to the start of each  
310 season to meet this definition. Any overall bias in the total observed charge can be absorbed into

311 an efficiency term, such as the quantum efficiency. This is valid since the linearity between the  
312 instantaneous total charge collected and the number of incident photons is satisfied up to  $\sim 2$  V [9],  
313 or approximately 560 PE. That is, the average charge collected from  $N$  photons is  $N$  times the  
314 average charge of the SPE charge distribution, and the average charge of the SPE charge distribution  
315 is always a set fraction of the Gaussian mean.

## 316 1.2 IceCube datasets and software definitions

317 The amount of observed light depends on the local properties of the ice [6]. Short term climate  
318 variations from volcanoes and longer-term variations from atmospheric dust affect the optical  
319 properties of the ice, producing nearly horizontal layers. This layered structure affects how much  
320 light the DOMs observe, and, with it, the trigger rate. The largest contribution to the IceCube trigger  
321 rate comes from downward-going muons produced in cosmic ray-induced showers [21]. Cosmic  
322 ray muons stopping in the detector cause the individual trigger rates to decrease at lower depths.

323 If a DOM and its nearest or next-to-nearest neighbor observe a discriminator threshold crossing  
324 within a set time window, a *Hard Local Coincidence* (HLC) is initiated, and the corresponding  
325 waveforms are sampled and read out on the three ATWD channels. Thermionic emission induced  
326 dark noise can be present in the readout, however it is suppressed at lower temperatures and is  
327 unlikely to trigger an HLC event.

328 After waveform digitization, there is a correction applied to remove measured baseline offsets.  
329 Distortions to the waveform, such as from droop and undershoot [8] introduced by the toroidal  
330 transformer AC coupling are compensated for in software during waveform calibration by adding  
331 the expected reaction voltage of the distortion to the calibrated waveform. If the undershoot  
332 voltage drops below 0 ADC counts, the ADC values are zeroed and then compensated for once  
333 the waveform is above the minimum ADC input. For each version of the AC coupling, scaled  
334 single photoelectron pulse shapes are then fit to the digitized waveforms using software referred to  
335 as "WaveDeform" (waveform unfolding process), which determines the individual pulse times and  
336 charges and populates a pulse series.

337 The pulse series used in this analysis come from two datasets:

- 338 1. The **MinBias dataset**. This dataset preserves the full waveform readout of randomly-selected  
339 HLC events, collecting on average 1:1000 events. The largest contribution to this dataset  
340 comes from downward-going muons produced in cosmic-ray-induced showers. The average  
341 event for this sample is approximately 26 PE bright and distributed over an average of 16  
342 triggered DOMs. The full waveform of these events allows us to extract the raw information  
343 about the individual pulses. This dataset will be used to measure the individual PMT charge  
344 distributions.
- 345 2. The **BeaconLaunch dataset**. This dataset is populated with digitized waveforms that are ini-  
346 tiated by the electronics (forced-triggered) of a channel that has not gone above the threshold.  
347 The forced triggered waveforms are typically used to monitor the individual DOM baselines  
348 and thus includes the full ATWD waveform readout. Since this dataset is forced-triggered, the  
349 majority of these waveforms represent electronic noise with minimal contamination from ran-  
350 dom accidental coincidence SPEs. This dataset will be used to examine the noise contribution  
351 to the charge distributions.

352 When using this dataset, the weight of every pulse is multiplied by a factor of 28.4 to account  
353 for the livetime difference between the MinBias dataset and the BeaconLaunch dataset.  
354 Weight, in this context, refers to the number of photons in the MinBias dataset proportional  
355 to one statistical photon in the BeaconLaunch dataset for which both datasets have the same  
356 equivalent livetime.

357 This analysis uses the full MinBias and BeaconLaunch datasets from IceCube seasons 2011 to  
358 2016 [22], subsequently referred to as IC86.2011 to IC86.2016. Seasons in IceCube typically start  
359 in May of the labeled year and end approximately one year later. Calibration is performed before  
360 the start of each season.

## 361 **2 Extracting the SPE charge templates**

### 362 **2.1 Single photoelectron pulse selection**

363 The pulse selection is the method used to extract candidate, unbiased, single photoelectron pulses  
364 from high-gain ATWD channel while minimizing the MPE contamination. The pulse selection was  
365 designed such that it avoids collecting afterpulses, does not include late pulses from the trigger,  
366 accounts for the discriminator threshold, reduces the effect of signal droop and undershoot, and  
367 gives sufficient statistics to perform a season-to-season measurement. An illustrative diagram of  
368 the pulse selection is shown in the left side of Fig. 2, while a description of the procedure is detailed  
369 below.

370 We restrict the pulse selection to only extract information from waveforms in which the trigger  
371 pulse does not exceed 10 mV ( $\sim 2$  PE) and no subsequent part of the waveform exceeds 20 mV  
372 ( $\sim 4$  PE). This reduces the effect of the baseline undershoot due to the AC coupling or other artifacts  
373 from large pulses.

374 In order to trigger a DOM, the input to the front-end amplifiers must exceed the discriminator  
375 threshold. To avoid the selection bias of the discriminator trigger (i.e. only selecting pulses greater  
376 than the discriminator threshold), we ignore the trigger pulse as well as the entire first 100 ns of the  
377 time window. Ignoring the first 100 ns removes late pulses that could be attributed to the triggering  
378 pulse, which occurs approximately 4% of the time [8]. To ensure we are not accepting afterpulses  
379 into the selection, we also enforce the constraint that the pulse of interest (POI) is within the first  
380 375 ns of the ATWD time window. This also allows us to examine the waveform up to 50 ns after  
381 the POI. In the vicinity of the POI, we ensure that WaveDeform did not reconstruct any pulses up  
382 to 50 ns prior to the POI, or 100 to 150 ns after the POI (the light gray region of Fig. 2 (left)). This  
383 latter constraint is to reduce the probability of accidentally splitting a late pulse in the summation  
384 window.

385 If a pulse is reconstructed between 100 and 375 ns after the start of the waveform and the voltage  
386 criteria are met, it is accepted as a candidate photoelectron and several checks are performed on  
387 the waveform prior to and after the pulse. The first check is to ensure that the waveform is near the  
388 baseline just before the rising edge of the POI. This is accomplished by ensuring that the waveform  
389 does not exceed 1 mV, 50 to 20 ns prior to the POI, and eliminates cases where the POI is a late  
390 pulse. We also ensure the waveform returns to the baseline by checking that no ADC measurement

391 exceeds 1 mV, 100 to 150 ns after the POI. These constraints are illustrated as the horizontal red  
 392 dotted lines and black arrows in the left side of Fig. 2.

393 If all the above criteria are met, we sum the reconstructed charges from the POI time, given by  
 394 WaveDeform, to +100 ns (the dark gray area in Fig. 2 (left)). This ensures that any nearby pulses are  
 395 either fully separated or fully added. This is important since WaveDeform may occasionally split  
 396 an SPE pulse into multiple smaller pulses, therefore it is always critical to perform a summation of  
 397 the charge within a time window. The 100 ns summation also implies that the pulse selection will  
 398 occasionally accept MPE events. We chose 100 ns window for the summation to ensure that we  
 399 collect the charge of the late pulse (recall that late pulses were measured up to 70 ns after the main  
 400 pulse), should it be there, while minimizing the MPE contamination. We estimate that there is on  
 401 average a 6.5% probability of the summation time window includes two or more photons.

## 402 2.2 Characterizing the low-charge region

403 This analysis aims to describe the full SPE charge distribution for each DOM. This is required by  
 404 the IceCube simulation. However, we cannot extract charge to arbitrary low PE before electronic  
 405 noise starts dominating. The aim of this section is to describe how we extract information in the  
 406 low-charge region (below 0.25 PE) to guide the full fit. Fig. 2 (right) shows the charge distributions  
 407 of the selected pulses that pass the single photoelectron pulse selection for string 1, optical module  
 408 1, DOM(1,1). In the low-charge region, we see a second threshold at approximately 0.13 PE, i.e. the  
 409 charge distribution terminates. This threshold arises from a termination condition in WaveDeform,

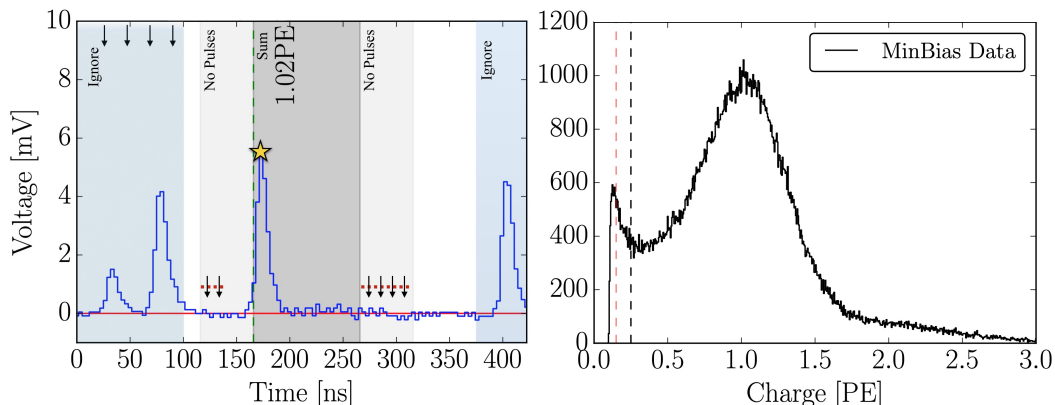


**Figure 2.** Left: An illustrative diagram of the pulse selection criteria for selecting a high-purity and unbiased sample of single photoelectrons. An example digitized ATWD waveform of data is shown in blue and the baseline is shown as a solid red line. The pulse of interest is identified with a yellow star. This example waveform was triggered by a small pulse at 25 ns (recall that the delay board allows us to examine the waveform just prior to the trigger pulse), followed by a potential late pulse at 70 ns. At 400 ns, we see a pulse in the region susceptible to afterpulses. Waveform voltage checks are illustrated with arrows, and various time windows described in the text are drawn with semi-opaque regions. The pulse of interest (POI) is reported to have a charge of 1.02 PE, given by WaveDeform, and would pass the pulse selection criteria. Right: The collected charge distribution from string 1, optical module 1 (DOM 1,1), from the MinBias dataset collected from IC86.2011 to IC86.2016 that pass the pulse selection. The red dashed line and black dotted line indicate 0.15 PE and 0.25 PE respectively. The pulse selection access charges below the discriminator threshold of 0.23 PE. The fall off in charge around 0.13 PE is due to the software defined threshold from WaveDeform.

410 in which the pulses that are smaller than predefined criteria are rejected. The threshold was set to  
 411 avoid electronic noise being interpreted as PMT pulses and contaminating the low-charge region.

412 The steeply falling component of the region from 0.13 PE to 0.25 PE is in agreement with  
 413 the laser measurements mentioned in Sec. 1.1 and emphasizes the importance of collecting data  
 414 below the discriminator threshold. This section will assess the noise contribution to this region and  
 415 examine the effect on the charge distribution and noise contribution by lowering the WaveDeform  
 416 threshold.

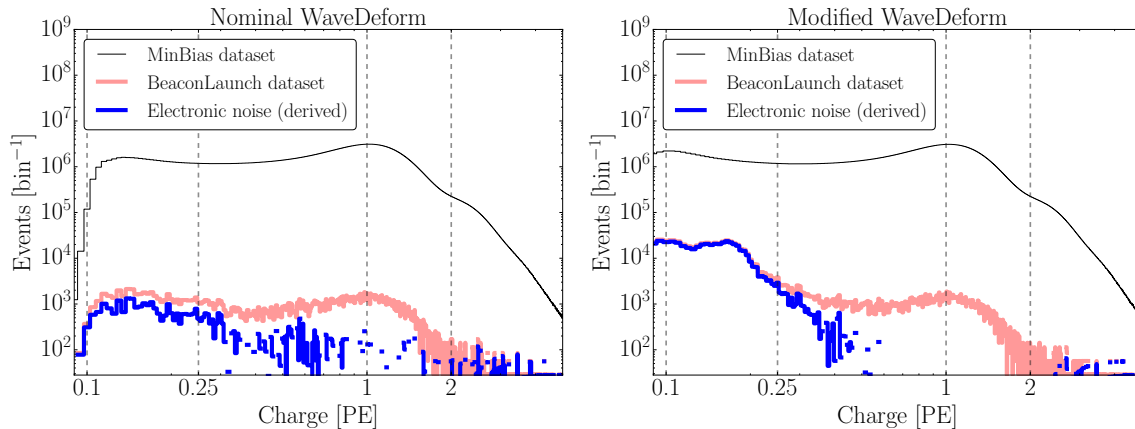


**Figure 3.** The cumulative charge distributions of all DOMs for the MinBias (M) and BeaconLaunch (B) datasets. The blue histogram shows the derived contribution from electronic noise. This was found by subtracting the normalized MinBias dataset from the BeaconLaunch dataset ( $B - M \times (B|_{1PE}/M|_{1PE})$ ). Left: The charge distributions for the standard WaveDeform settings. Right: The charge distributions for the modified WaveDeform settings.

417 Fig. 3 (left) shows the charge distributions for the MinBias (black) and the BeaconLaunch  
 418 (red) datasets using the default settings of WaveDeform (standard WaveDeform). As mentioned  
 419 in Sec. 1.2, occasionally a photoelectron will be coincident with the forced BeaconLaunch time  
 420 window. These charges populate a SPE charge distribution. Subtracting the shape of the MinBias  
 421 charge distribution from the BeaconLaunch dataset yields an estimate of the amount of electronic  
 422 noise contamination (blue). The bin in the MinBias data with the lowest signal-to-noise ratio (SNR)  
 423 above 0.1 PE was found to have a SNR of 744.7. The SNR for the full distribution was found to be  
 424  $1.98 \times 10^5$ . Fig. 3 (right) shows the same data after lowering the WaveDeform threshold (modified  
 425 WaveDeform), and is found to have SNR of 57.9 in the bin with the largest contamination and the  
 426 total SNR was found to be  $0.69 \times 10^5$ .

427 The modified WaveDeform datasets show a minimal increase in the contribution of noise to  
 428 the low-charge region. From this, however, we are able to extract charge information down to  
 429 approximately 0.10 PE and improve the overall description of the charge distribution below the  
 430 discriminator. This will help constrain the values of the steeply falling exponential, defined with  
 431  $\text{Exp}_1$ .

### 432 **2.3 Fitting procedure**

433 We would now like to fit the charge distribution to extract the SPE charge templates (the components  
434 of Eq. 1.1) for all DOMs.

435 Contamination from two-photon events is suppressed by the pulse selection, but can not be  
436 entirely avoided. To minimize potential biases by the charge entries resulting from two photons,  
437 the one and two photon contribution to the charge distributions is fitted at the same time, using  
438 something we call a convolutional fitter. It assumes that the charge distribution resulting from two  
439 photons is the SPE charge distribution convolved with itself [23]. In each step of the minimizer the  
440 convolution is updated given the current set of SPE parameters to be evaluated and the relative one  
441 and two photon contributions is determined.

442 We do not account for the three-photon contribution, which is justified by the lack of statistics  
443 in the 3 PE region as well as the significant rate difference between the 1 PE and 2 PE region, as  
444 shown in Fig. 2 (right).

445 Pulses that fall below the WaveDeform threshold and are not reconstructed contribute to an  
446 inefficiency in the individual DOMs. That is, the shape below the WaveDeform software threshold  
447 does not have a significant impact, but the relative area of the SPE charge template below compared  
448 to above this threshold changes the efficiency of the DOM. This analysis assumes the same shape  
449 of the steeply falling exponential component ( $\text{Exp}_1$ ) for all DOMs in the detector to avoid large  
450 fluctuations in the DOM-to-DOM efficiencies. The modified WaveDeform data will strictly be  
451 used to determine the  $\text{Exp}_1$  component. Specifically, using the aggregate of the entire ensemble  
452 of DOMs with the modified WaveDeform dataset, we background-subtract the BeaconLaunch  
453 distribution from the MinBias data, fit the resulting distribution to determine the components of  
454 Eq. 1.1, and use only the measured shape and normalization of  $\text{Exp}_1$  in all subsequent standard  
455 WaveDeform fits.

456 As described in Sec. 1.1, the Gaussian mean ( $\mu$ ) is used to determine the gain setting for  
457 each PMT. Therefore, it is particularly important that the fit quality in the peak region accurately  
458 describes the data. While fitting to the full charge distribution improves the overall fit agreement,  
459 the mismatch between the chosen functional form (Eq. 1.1) and a true SPE charge distribution can  
460 cause the Gaussian component to pull away from its ideal location. To compensate for this, the  
461 fitting algorithm prioritizes fitting to the data around the Gaussian mean. This is accomplished by  
462 first fitting to the full distribution to get an estimate of the Gaussian mean location. Then, the data  
463 in the region  $\pm 0.15$  PE around the original estimated Gaussian mean is weighted to have a higher  
464 impact on the fit, and the distribution is re-fitted.

465 Upon fitting the MinBias dataset with the predetermined values for  $\text{Exp}_1$ , the residual of each  
466 fit is calculated by measuring the percentage difference between the fit and the data. The average  
467 residual is then used as a global scaling factor for all SPE charge templates to account for the  
468 difference between the chosen model (Eq. 1.1) and the actual data.

### 469 **2.4 SPE charge template fit results**

470 We now present the results of the fits and describe the correlations of the fit parameters with hardware  
471 differences, and time variations in the next section. Using the background-subtracted modified  
472 WaveDeform dataset, the  $\text{Exp}_1$  component was determined by fitting the aggregate distribution

473 from 0.1 PE to 3.5 PE. The result of the fit yielded  $P_{e1} = 0.186 \pm 0.041$  and  $w_1 = 0.027 \pm 0.002$  PE.  
 474 This shape of  $\text{Exp}_1$  is now used to describe the low-PE charge region for all subsequent standard  
 475 WaveDeform fits.

476 Using the MinBias dataset with the measured val-  
 477 ues of  $\text{Exp}_1$ , the SPE charge templates are extracted for  
 478 every DOM, separately for each IceCube season from  
 479 IC86.2011 to IC86.2016. The fit range for  $\text{Exp}_2$  and the  
 480 Gaussian components is selected to be between 0.15 PE  
 481 and 3.5 PE. An average fit was also performed on the cu-  
 482 mulative charge distribution, in which all the data for a  
 483 given DOM was summed (labeled as "AVG").

484 All the DOMs with "failed fits" are not included in  
 485 this analysis. A DOM is classified as having a failed  
 486 fit if it does not pass one of the validity checks on the  
 487 data requirements (e.g. the number of valid pulses) or  
 488 goodness of fit. Over the seasons considered, between  
 489 107 and 111 DOMs have been excluded from service  
 490 (the white elements shown in Fig. 1) and represent the  
 491 majority of the failed fits. The remaining 6 DOMs that  
 492 failed the AVG fits are known to have various issues. In the IceCube MC simulation chain, these  
 493 DOMs are assigned the average SPE charge template.

494 We can divide the DOMs into subsets with the following hardware differences: the HQE DOMs  
 495 with the new toroids, the Standard QE DOMs with the new toroids, and the Standard QE DOMs  
 496 with the old toroids. The mean value and standard error of the IC86.AVG fit parameters, excluding  
 497  $\text{Exp}_1$ , for the subset of hardware differences are listed in Table 1. The residual, averaged over all  
 498 DOMs, from 0 to 1 PE is shown in Fig. 4.

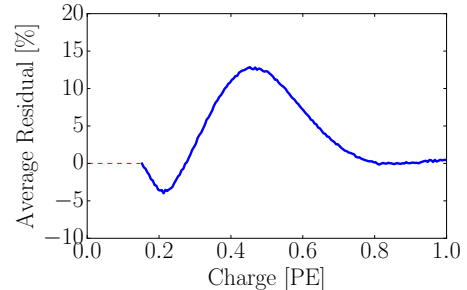


**Figure 4.** The extracted residual in blue, comparing the result of the convolutional fit to the data, averaged over all DOMs. The dashed red line indicates the region where we do not have sufficient data and therefore set the residual to 0% (i.e. no correction will be applied in this region).

Hardware	$\text{Exp}_2$ Prob. ( $P_{e1}$ )	$\text{Exp}_2$ Width ( $w_2$ )	Gaus. Prob. ( $1-P_{e1}-P_{e2}$ )	Gaus. Mean ( $\mu$ )	Gaus. Width ( $\sigma$ )
HQE / New Toroid	$0.243 \pm 0.002$	$0.354 \pm 0.004$	$0.570 \pm 0.002$	$1.0148 \pm 0.0011$	$0.312 \pm 0.002$
NQE / New Toroids	$0.210 \pm 0.001$	$0.344 \pm 0.001$	$0.604 \pm 0.001$	$1.0183 \pm 0.0004$	$0.316 \pm 0.001$
NQE / Old Toroids	$0.206 \pm 0.001$	$0.377 \pm 0.003$	$0.608 \pm 0.001$	$1.0030 \pm 0.0008$	$0.294 \pm 0.001$

**Table 1.** The average values and standard error of each fit parameter for the subset of hardware configurations listed in the first column.

499 An example fit is shown in Fig. 5 for the cumulative MinBias charge distribution for DOM  
 500 (1,1). The collected charge distribution is shown in the black histogram, while the fit to the data is  
 501 shown as the red line. The extracted SPE charge template from the fit is shown in blue. Both the fit  
 502 and extracted SPE charge template have been scaled by the average residual shown in Fig. 4.

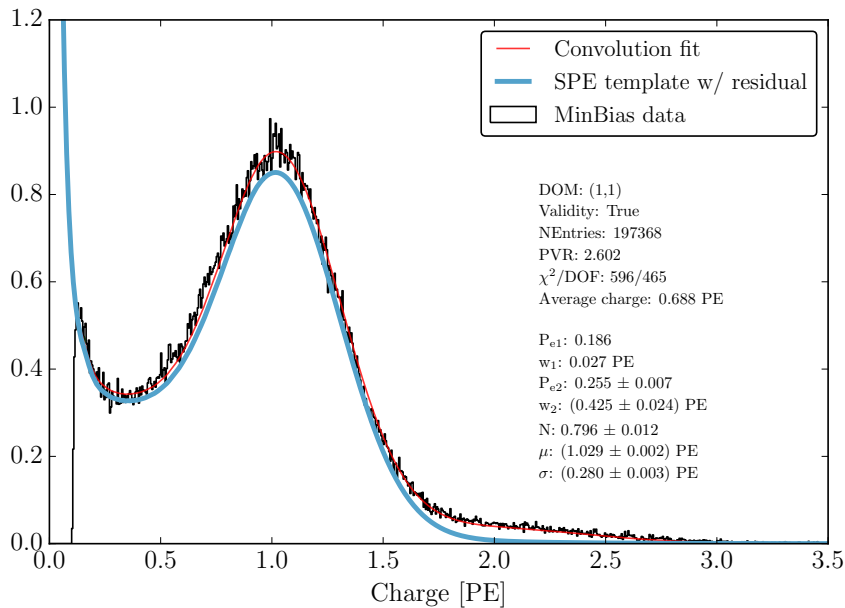


**Figure 5.** An example fit for DOM(1,1) using the MinBias dataset (black histogram) including data from seasons IC86.2011 to IC86.2016. The result of the convolution fit, which includes the 2 PE contribution, is shown as a solid red line and the extracted SPE charge template from the fit is shown in blue. For both the convolution fit and the SPE charge template, the curves include the correction from the average residual shown in Fig. 4. Here,  $P_{e1} = 0.186$  and  $w_1 = 0.027$  PE are fixed, as discussed at the end of Sec. 2.2.

### 503 3 Discussion

#### 504 3.1 Correlations between fit parameters and DOM hardware differences

505 It is evident from the data in Table 1 that the average shape of the SPE charge templates depends  
 506 on the DOM hardware. These differences can also be seen in the measured peak-to-valley ratios  
 507 and average charge of the SPE charge template (see Fig. 6). When we examine the subset of DOMs  
 508 instrumented with the new toroids, the average HQE DOM were found to have a  $20.2 \pm 0.6\%$  larger  
 509  $P_{e2}$  component and  $4.7 \pm 0.4\%$  smaller Gaussian width. Consequently, the average HQE peak-to-  
 510 valley ratio is measured to be  $2.255 \pm 0.012$ , or  $13.67 \pm 0.01\%$  lower than the average for Standard  
 511 QE DOMs. Also, the average charge of the average HQE DOM was found to be  $3.17 \pm 0.01\%$  lower  
 512 than that of the Standard QE DOMs. The average charge is calculated by integrating over the full  
 513 SPE charge template including the residual correction. The values shown in Fig. 6 (right) are found  
 514 to be below 1 PE due to the low-PE contribution from  $\text{Exp}_1$  and  $\text{Exp}_2$ , whose physical description  
 515 can be found in Sec. 1.1.

516 IceCube compensates for the change in the mean measured charge in simulation, by increasing  
 517 the HQE DOM efficiency by the equivalent amount. This ensures that the total amount of charge  
 518 collected by the HQE DOMs remains the same prior to, and after, inserting the SPE charge templates  
 519 into simulation.

520 Similarly, using only the subset of Standard QE DOMs, the SPE charge templates were  
 521 found to have measurably different shapes when comparing the different methods of AC coupling.

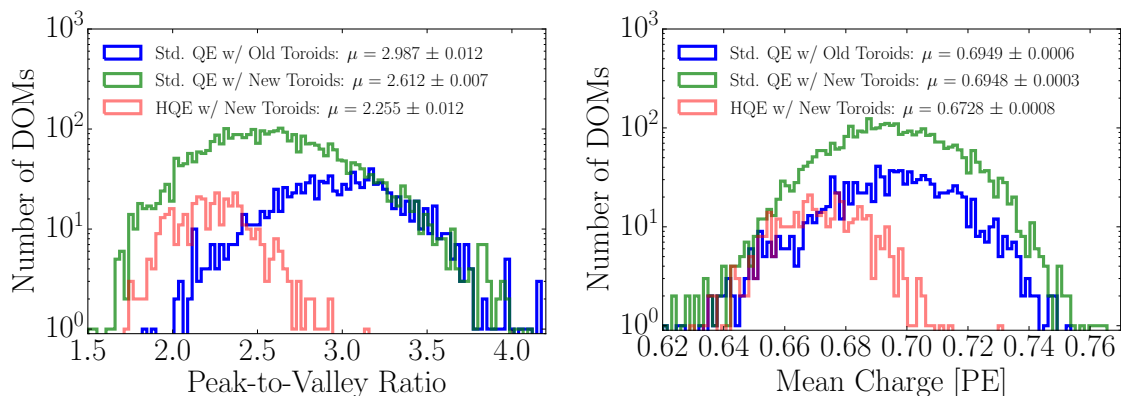


**Figure 6.** Comparison between the R7081-02MOD HQE DOMs and standard R7081-02 DOMs. Left: The peak-to-valley ratio for the two subsets of quantum efficiencies. Right: The average charge of the individual DOM SPE charge templates.

522 The average Gaussian width for the DOMs instrumented with the old toroids were found to be  
 523  $8.1 \pm 0.1\%$  narrower, albeit with a very similar probability of the photoelectron populating the  
 524 Gaussian component. With these differences, we find a peak-to-valley ratio of  $2.612 \pm 0.007$  for  
 525 the new toroid DOMs and  $2.987 \pm 0.012$  for the old toroid DOMs. The average Gaussian mean of  
 526 the fit for the DOMs with the old toroids was also found to be  $1.6 \pm 0.1\%$  lower than those with the  
 527 new toroids. This corresponds proportionally to a change in the expected gain. The average charge,  
 528 however, between these two hardware configurations is very similar,  $0.012 \pm 0.001\%$ .

529 Although the DOMs instrumented with the old toroids were deployed into the ice earlier than  
 530 those with the new toroids, the differences above remain when examining individual deployment  
 531 years; therefore, the shape differences are not attributed to the change in the DOM behavior over time.  
 532 However, the DOMs with the old toroids were the first PMTs to be manufactured by Hamamatsu.  
 533 A gradual change of the fit parameters was observed when ordering the PMTs according to their  
 534 PMT serial number (i.e. their manufacturing order). Fig. 7 shows the change in the measured  
 535 peak-to-valley ratio as a function of PMT serial number for the standard QE DOMs (blue) and HQE  
 536 PMTs (red). Here, each data point represents a single PMT and the blue (red) data points indicate  
 537 a PMT instrumented with the new (old) toroid. This is compelling evidence that the observed  
 538 differences between the new and old toroids is due to a change in the PMT production procedure  
 539 rather than version of AC coupling.

540 Fig. 8 illustrates the average shape differences in the extracted SPE charge templates between the  
 541 HQE DOM with the new toroids (solid white line), Standard QE with the new toroids (dotted white  
 542 line), Standard QE with the old toroids (dashed white line), compared to the spread in the measured  
 543 SPE charge templates for all DOMs in the detector (dark blue contours). The figure also shows  
 544 how the previous default SPE charge distribution, the TA0003 distribution, compares to this recent  
 545 measurement. All curves in this figure have been normalized such that the area above 0.25 PE is the  
 546 same. The observable shape differences from the TA0003 are attributed to a better understanding  
 547 of the low-charge region, the difference in functional form (described in Section 1.1), and the fact  
 548 that the SPE charge templates were generated using a realistic photocathode illumination.

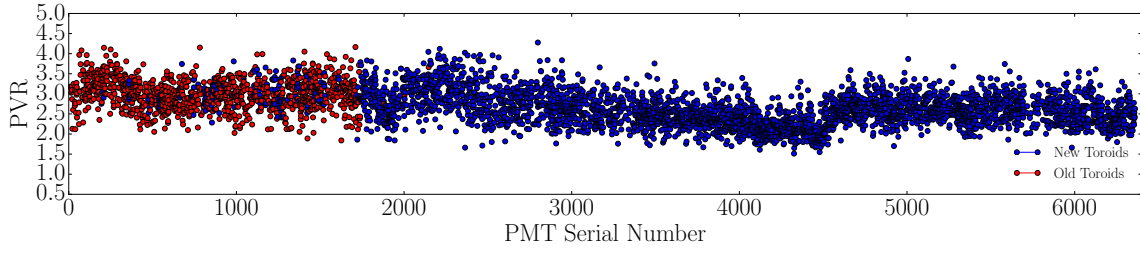


**Figure 7.** The measured peak-to-valley ratio for the standard QE PMTs ordered by PMT serial number. The red data points indicate a PMT instrumented with an old toroid, whereas new toroids are indicated by the blue data points.

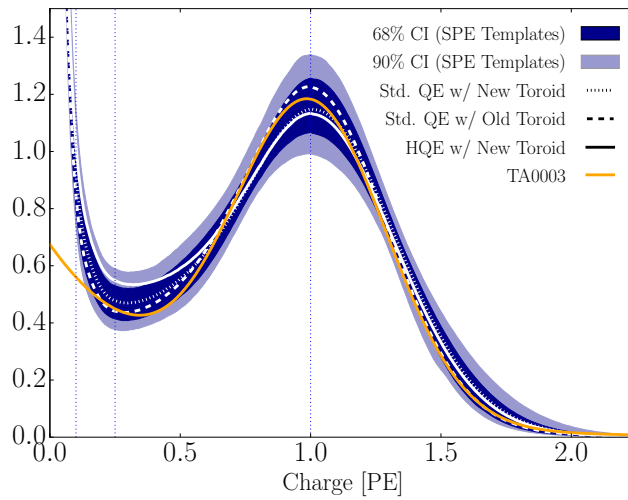


**Figure 8.** The inner (outer) dark blue region shows the 68% (90%) confidence interval defined by the measured spread in the extracted SPE charge templates of all DOMs in the detector. Superimposed are the average SPE charge templates for the variety of hardware configurations shown in white. The TA0003 distribution, for comparison, is shown in orange. All curves have been normalized such that the area above 0.25 PE is the same.

### 549 3.2 Fitting parameters variation over time

550 The SPE charge templates were extracted for each IceCube season independently so to investigate  
 551 the time dependence of the fit parameters. For every DOM in the detector, the change over time of  
 552 each fit parameter (excluding  $\text{Exp}_1$ ) was calculated. Fig. 9 shows the change in a given fit parameter,  
 553 relative to the mean value, per year. The measured distributions were found to be consistent with  
 554 randomly scrambling the order of each seasonal measurement. The largest deviation was found to  
 555 be average of each fit parameters are found to deviate less than 0.1%, which is in agreement with the  
 556 stability checks performed in Ref. [9]. This observation holds for the individual subsets of DOMs  
 557 with different hardware configurations as well.

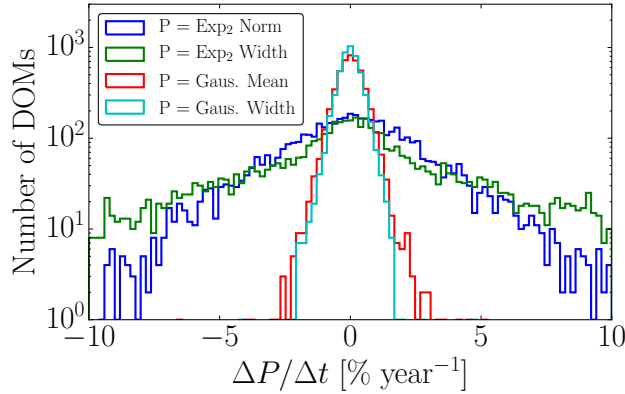


**Figure 9.** The change in the individual DOM fitted parameters over the six seasons of data. The histogram represents the rate of change, per season, of the fitted parameter labelled in the legend.

### 558 3.3 Quantifying observable changes when modifying the PMT charge distributions

559 Changing the assumed gain response in simulation has different implications depending on the  
 560 typical illumination level present in different analyses. These differences are outlined in the  
 561 following discussion.

562 The PMT response is described by a combination of a "bare" efficiency,  $\eta_0$ , and a normalized  
 563 charge response function,  $f(q)$ . The bare efficiency represents the fraction of arriving photons  
 564 that result in any nonzero charge response, including those below the discriminator threshold. The  
 565 normalization condition is:

$$\int_0^{\infty} f(q) dq = 1. \quad (3.1)$$

566 Generally,  $f(q)$  and  $\eta_0$  have to be adjusted together to maintain agreement with a quantity known  
 567 from lab or in-ice measurements, such as the predicted number of pulses above threshold for a dim  
 568 source.

569 **Dim source measurements** Where light levels are low enough, the low occupancy ensures that  
 570 sub-discriminator pulses do not contribute to any observed charge as they do not satisfy the trigger  
 571 threshold. Given some independent way of knowing the number of arriving photons, a lab or in-ice  
 572 measurement determines the trigger fraction above threshold  $\eta_{0.25}$  and/or the average charge over  
 573 threshold  $Q_{0.25}$ , either of which can be used to constrain the model as follows:

$$\eta_{0.25} = \eta_0 \int_{0.25q_{pk}}^{\infty} f(q) dq \quad (3.2)$$

$$Q_{0.25} = \eta_0 \int_{0.25q_{pk}}^{\infty} q f(q) dq \quad (3.3)$$

574 Here, the discriminator threshold is assumed to be 0.25 times the peak position  $q_{pk}$ . It is also  
 575 useful to multiply observed charges by  $q_{pk}$ , since we set each PMT gain by such a reference, and  
 576 then a measurement constraint would be stated in terms of  $Q_{0.25}/q_{pk}$ .

577 **Semi-bright source measurements** For semi-bright sources, pulses that arrive after the readout  
578 time window is opened are not subject to the discriminator threshold. WaveDeform introduces  
579 a software termination condition at  $\sim 0.13$  PE (described at the end of Section 2.1). The average  
580 charge of an individual pulse that arrives within the time window is:

$$Q_{0.10} = \eta_0 \int_{0.10q_{pk}}^{\infty} qf(q)dq \quad (3.4)$$

581 **Bright source measurements** For light levels that are large, the trigger is satisfied regardless  
582 of the response to individual photons, and the total charge per arriving photon therefore includes  
583 contributions below both the discriminator and the WaveDeform thresholds:

$$Q_0 = \eta_0 \int_0^{\infty} qf(q)dq \quad (3.5)$$

584 As such, the total charge is directly proportional to the average charge of the SPE charge  
585 template.

### 586 3.3.1 Model comparison

587 A natural question to ask is whether or not a change in  $f(q)$  would cause observable changes in the  
588 bright-to-dim ratios. That is, when we change the SPE charge distribution in simulation, should  
589 we expect the charge collected by bright events compared to dim events to change? When the  
590 charge distribution model is changed in a way that preserves agreement with the measured  $\eta_{0.25}$  or  
591  $Q_{0.25}/q_{pk}$ , i.e.  $\eta_0$  is adjusted properly for changes in  $f(q)$ , the physical effect can be summarized  
592 by the change in the bright-to-dim ratios  $Q_0/Q_{0.25}$ , and  $Q_0/Q_{0.10}$ . Conveniently, these ratios depend  
593 only on the shape of  $f(q)$ . Table 2 compares these ratios in terms of the TA0003 charge distribution  
594 and the SPE charge templates described here. It is shown that there are sub-percent level differences  
595 in the physically-observable bright-to-dim ratios. The largest difference in the shape between the  
596 SPE charge templates and the TA0003 distribution is in the low-charge region, particularly below  
597  $\sim 0.10$  PE. Charge from this region can only inflate bright events. That is, these pulses are small to  
598 trigger the discriminator or be reconstructed by WaveDeform, however they can reside on top of  
599 other pulses, inflating them. Since these pulses by definition contain little charge, they do not tend  
600 to inflate the measured charge by a noticeable amount, as shown by the  $Q_0/Q_{0.25}$  measurements in  
601 Table 2.

Model	Detector	$Q_0/Q_{0.25}$	$Q_0/Q_{0.10}$	$\eta_{0.25}/Q_{0.25}$
TA0003	All DOMs	1.017	1.003	1.050
SPE Templates	HQE + New Toroids	1.022±0.002	1.004±0.001	1.050±0.017
SPE Templates	NQE + New Toroids	1.019±0.002	1.004±0.001	1.034±0.018
SPE Templates	NQE + Old Toroids	1.017±0.002	1.003±0.001	1.048±0.023

**Table 2.** The distribution in bright-to-dim ratios for the previous charge distribution (TA0003) and the individual DOM SPE charge templates for the IceCube and DeepCore detectors.

### 602 **3.4 SPE charge templates for calibration**

603 The gain setting on each PMT is calibrated prior to the beginning of each season such that the  
604 Gaussian mean of the charge distribution corresponds to a gain of  $10^7$ , or equivalently 1 PE.  
605 This gain calibration method, run directly on the DOMs, uses waveform integration for charge  
606 determination instead of WaveDeform unfolding, resulting in a small systematic shift in gain. This  
607 systematic shift was determined for every PMT. The mean shift obtained over all DOM was found  
608 to be  $1.47 \pm 0.04\%$  with a standard deviation of  $2.62\%$ , corresponding to an overestimation of the  
609 measured charge in the detector.

610 The correction to the systematic shift in the measured charge can be implemented retroactively  
611 by dividing the reported charge from WaveDeform by the corresponding offset for a given DOM.  
612 Alternatively, we can account for this by simply inserting SPE charge templates, measured in this  
613 analysis, into simulation such that the corresponding systematic shift is also modeled in simulation.  
614 This will be performed in the following subsection.

### 615 **3.5 SPE charge templates in simulation**

616 To model the IceCube instrument, we must implement the PMT response in simulation. The  
617 IceCube MC simulation chain assigns a charge to every photoelectron generated at the surface of  
618 the photocathode. The charge is determined by sampling from a normalized charge distribution  
619 probability density function (PDF). A comparison to data between describing the charge distribution  
620 PDF using the SPE charge templates and the TA0003 distribution follows.

621 Two simulation sets consisting of the same events were processed through the IceCube Monte  
622 Carlo simulation chain to the final analysis level of an update to the IC86.2011 sterile neutrino analy-  
623 sis [24]. Here, the events that pass the cuts are  $>99.9\%$  upward-going (a trajectory oriented upwards  
624 relative to the horizon) secondary muons produced by charged current muon neutrino/antineutrino  
625 interactions. The muon reconstructed energy range of this event selection is between approximately  
626 500 GeV and 10 TeV.

627 Fig. 10 (left) shows the distribution of the total measured charge during each event per DOM  
628 (data points). The simulation set using the TA0003 charge distribution is shown in orange, and that  
629 using the SPE charge templates is shown in blue. The data is shown for the full IC86.2012 season  
630 but is statistically equivalent to any of the other seasons. Fig. 10 (right) shows the distribution of  
631 the total measured charge of an event divided by the number of channels (NChan), or DOMs, that  
632 participated in the event. Both plots in Fig. 10 have been normalized such that the area under the  
633 histograms is the same.

634 The SPE charge templates clearly improve the overall MC description of these two variables.  
635 This update may be useful for analyses that rely on low-occupancy events (low-energy or dim  
636 events) in which average charge per channels is below 1.5 PE, and will be investigated further  
637 within IceCube.

## 638 **4 Conclusion**

639 This article outlines the procedure used to extract the SPE charge templates for all in-ice DOMs in  
640 the IceCube detector using in-situ data from IC86.2011 to IC86.2016. The SPE charge templates

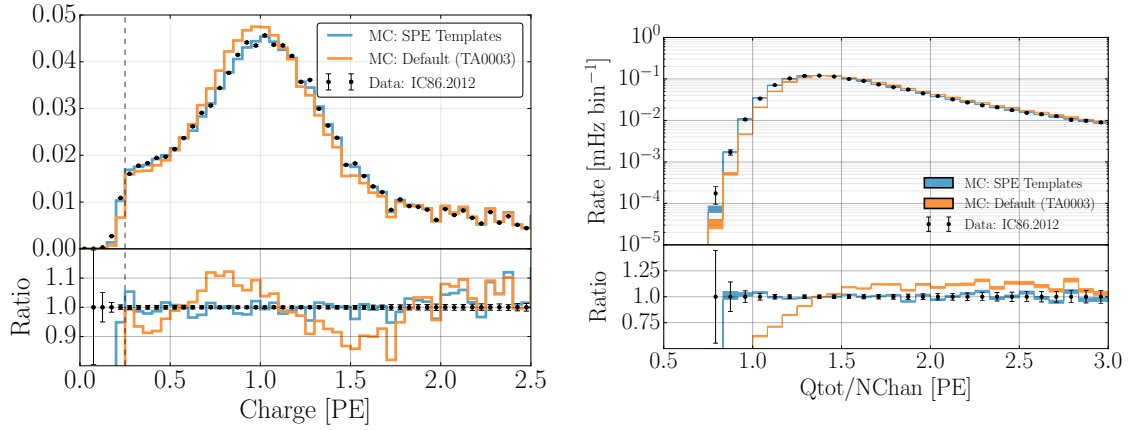


**Figure 10.** A comparison between the SPE charge templates (blue) and the TA0003 (orange) model for describing the SPE charge distribution in Monte Carlo. The simulation is compared to the 2012 IceCube season. The data is shown in black. Left: The total measured charge per DOM, per event at analysis level. Right: The distribution of the total measured charge of an event divided by the number of DOMs that participated in the event.

641 represent an update to the modeled single photoelectron charge distribution previous used by  
 642 IceCube, the TA0003 distribution. The result of this measurement was shown to be useful for  
 643 improving the overall data/MC agreement as well as calibration of the individual PMTs. It also  
 644 prompted a comparison between the shape of the SPE charge templates for a variety of hardware  
 645 configurations and time dependent correlations.

646 The subset of HQE DOMs were found to have a smaller peak-to-valley ratio relative to the  
 647 Standard QE DOMs, as well as an overall  $3.17 \pm 0.01\%$  lower average charge. It was also found that  
 648 the DOMs instrumented with the old toroids used for AC coupling (the first PMTs to be manufactured  
 649 by Hamamatsu) had narrower Gaussian component corresponding in an average increased peak-to-  
 650 valley ratio of  $14.36 \pm 0.01\%$ . By assuming a relationship between the production time and serial  
 651 number, this difference was shown to be likely due to a change in the manufacturing over time  
 652 rather than the actual AC coupling method. No significant time dependence in any of the fitted  
 653 parameters associated with the SPE charge templates over the investigated seasons was observed.  
 654 A reassessment of the PMT gain settings found a systematic bias of  $1.47 \pm 0.04\%$  with a standard  
 655 deviation of  $2.62\%$ .

656 The SPE charge templates were inserted into the MC simulation and the results were compared  
 657 to the default TA0003 distribution. A significant improvement in the description of the variables  
 658 total charge per DOM and total charge over the number of channels was shown. Analyses which rely  
 659 on low-light occupancy measurements, will benefit from this update. As shown in the bright-to-dim  
 660 ratios, the average charge for various light levels will not be affected by this update.

## 661 **Acknowledgments**

662 We acknowledge the support from the following agencies:

663 USA – U.S. National Science Foundation-Office of Polar Programs, U.S. National Science  
664 Foundation-Physics Division, Wisconsin Alumni Research Foundation, Center for High Throughput  
665 Computing (CHTC) at the University of Wisconsin-Madison, Open Science Grid (OSG), Extreme  
666 Science and Engineering Discovery Environment (XSEDE), U.S. Department of Energy-National  
667 Energy Research Scientific Computing Center, Particle astrophysics research computing center at  
668 the University of Maryland, Institute for Cyber-Enabled Research at Michigan State University, and  
669 Astroparticle physics computational facility at Marquette University; Belgium – Funds for Scien-  
670 tific Research (FRS-FNRS and FWO), FWO Odysseus and Big Science programmes, and Belgian  
671 Federal Science Policy Office (Belspo); Germany – Bundesministerium für Bildung und Forschung  
672 (BMBF), Deutsche Forschungsgemeinschaft (DFG), Helmholtz Alliance for Astroparticle Physics  
673 (HAP), Initiative and Networking Fund of the Helmholtz Association, Deutsches Elektronen Syn-  
674 chrotron (DESY), and High Performance Computing cluster of the RWTH Aachen; Sweden –  
675 Swedish Research Council, Swedish Polar Research Secretariat, Swedish National Infrastructure  
676 for Computing (SNIC), and Knut and Alice Wallenberg Foundation; Australia – Australian Re-  
677 search Council; Canada – Natural Sciences and Engineering Research Council of Canada, Calcul  
678 Québec, Compute Ontario, Canada Foundation for Innovation, WestGrid, and Compute Canada;  
679 Denmark – Villum Fonden, Danish National Research Foundation (DNRF), Carlsberg Foundation;  
680 New Zealand – Marsden Fund; Japan – Japan Society for Promotion of Science (JSPS) and Institute  
681 for Global Prominent Research (IGPR) of Chiba University; Korea – National Research Foundation  
682 of Korea (NRF); Switzerland – Swiss National Science Foundation (SNSF); United Kingdom –  
683 Department of Physics, University of Oxford.

684 **References**

- 685 [1] J. Ahrens et al., *IceCube preliminary design document*, URL:  
686 <https://icecube.wisc.edu/icecube/static/reports/IceCubeDesignDoc.pdf> (2001) .
- 687 [2] A. Achterberg et al., *First year performance of the IceCube neutrino telescope*, *Astroparticle Physics*  
688 **26** (2006) 155–173, [[arXiv:astro-ph/0604450v2](https://arxiv.org/abs/astro-ph/0604450v2)].
- 689 [3] M. G. Aartsen et al., *Evidence for high-energy extraterrestrial neutrinos at the IceCube detector*,  
690 *Science* **342** (2013) 1242856, [[arXiv:1311.5238v2](https://arxiv.org/abs/1311.5238v2)].
- 691 [4] R. Abbasi et al., *The design and performance of IceCube DeepCore*, *Astroparticle Physics* **35** (2012)  
692 615–624, [[arXiv:1109.6096v1](https://arxiv.org/abs/1109.6096v1)].
- 693 [5] R. Abbasi et al., *The IceCube data acquisition system: Signal capture, digitization, and timestamping*,  
694 *NIM-A* **601** (2009) 294–316, [[arXiv:0810.4930v2](https://arxiv.org/abs/0810.4930v2)].
- 695 [6] M. Aartsen et al., *Measurement of South Pole ice transparency with the IceCube LED calibration*  
696 *system*, *NIM-A* **711** (2013) 73–89, [[arXiv:1301.5361v1](https://arxiv.org/abs/1301.5361v1)].
- 697 [7] R. Abbasi et al., *IceTop: The surface component of IceCube*, *NIM-A* **700** (2013) 188–220.
- 698 [8] R. Abbasi et al., *Calibration and characterization of the IceCube photomultiplier tube*, *NIM-A* **618**  
699 (2010) 139–152, [[arXiv:1002.2442v1](https://arxiv.org/abs/1002.2442v1)].
- 700 [9] M. G. Aartsen et al., *The IceCube Neutrino Observatory: Instrumentation and Online Systems*, *JINST*  
701 **12** (2017) 1748–0221, [[arXiv:1612.05093v2](https://arxiv.org/abs/1612.05093v2)].
- 702 [10] M. Aartsen et al., *Energy reconstruction methods in the IceCube Neutrino Telescope*, *JINST* **9** (2014)  
703 1748–0221, [[arXiv:1311.4767v3](https://arxiv.org/abs/1311.4767v3)].
- 704 [11] R. Stokstad, *Design and performance of the IceCube electronics*,  
705 URL: <https://cds.cern.ch/record/920022/files/p20.pdf> (2005) .
- 706 [12] Hamamatsu, *Resources: Basics and Applications*,  
707 URL: [https://www.hamamatsu.com/resources/pdf/etd/PMT\\_handbook\\_v3aE.pdf](https://www.hamamatsu.com/resources/pdf/etd/PMT_handbook_v3aE.pdf) (2018) .
- 708 [13] Hamamatsu, *Handbook Resources, Chapter 4*, URL: [https://www.hamamatsu.com/resources/pdf/etd/PMT\\_handbook\\_v3aE-Chapter4.pdf](https://www.hamamatsu.com/resources/pdf/etd/PMT_handbook_v3aE-Chapter4.pdf) (2018) .  
709
- 710 [14] J. Brack et al., *Characterization of the Hamamatsu R11780 12 in. photomultiplier tube*, *NIM-A* **712**  
711 (2013) 162–173, [[arXiv:1210.2765v2](https://arxiv.org/abs/1210.2765v2)].
- 712 [15] E. Calvo et al., *Characterization of large-area photomultipliers under low magnetic fields: Design*  
713 *and performance of the magnetic shielding for the Double Chooz neutrino experiment*, *NIM-A* **621**  
714 (2010) 222–230, [[arXiv:0905.3246v1](https://arxiv.org/abs/0905.3246v1)].
- 715 [16] F. Kaether and C. Langbrandtner, *Transit time and charge correlations of single photoelectron events*  
716 *in R7081 photomultiplier tubes*, *JINST* **7** (2012) P09002, [[arXiv:1207.0378v2](https://arxiv.org/abs/1207.0378v2)].
- 717 [17] B. Lubsandorzhev, P. Pokhil, R. Vasiljev and A. Wright, *Studies of prepulses and late pulses in the 8"*  
718 *electron tubes series of photomultipliers*, *NIM-A* **442** (2000) 452–458.
- 719 [18] K. Ma et al., *Time and amplitude of afterpulse measured with a large size photomultiplier tube*,  
720 *NIM-A* **629** (2011) 93–100, [[arXiv:0911.5336v1](https://arxiv.org/abs/0911.5336v1)].
- 721 [19] S. Torre, T. Antonioli and P. Benetti, *Study of afterpulse effects in photomultipliers*, *Review of*  
722 *Scientific Instruments* **54** (1983) 1777–1780.
- 723 [20] Hamamatsu, *Photomultiplier tubes: Construction and Operating Characteristics*,  
724 URL: [https://www.hamamatsu.com/resources/pdf/etd/PMT\\_TPMZ0002E.pdf](https://www.hamamatsu.com/resources/pdf/etd/PMT_TPMZ0002E.pdf) (2016) .

- 725 [21] M. Aartsen et al., *Characterization of the atmospheric muon flux in IceCube*, *Astroparticle Physics* **78**  
726 (2016) 1–27, [[arXiv:1506.07981v2](#)].
- 727 [22] M. Aartsen et al., *Search for steady point-like sources in the astrophysical muon neutrino flux with 8*  
728 *years of IceCube data*, *The European Physical Journal C* **79** (2019) 234, [[arXiv:1811.07979v2](#)].
- 729 [23] R. Dossi, A. Ianni, G. Ranucci and O. J. Smirnov, *Methods for precise photoelectron counting with*  
730 *photomultipliers*, *NIM-A* **451** (2000) 623–637.
- 731 [24] M. Aartsen et al., *Searches for sterile neutrinos with the IceCube detector*, *Physical Review Letters*  
732 **117** (2016) 071801, [[arXiv:1605.01990v2](#)].